

# Continuous Urban Change Detection from Satellite Image Time Series with Temporal Feature Refinement and Multi-Task Integration

Sebastian Hafner, Heng Fang, Hossein Azizpour and Yifang Ban\*, *Senior Member, IEEE*

**Abstract**—Urbanization advances at unprecedented rates, resulting in negative effects on the environment and human well-being. Remote sensing has the potential to mitigate these effects by supporting sustainable development strategies with accurate information on urban growth. Deep learning-based methods have achieved promising urban change detection results from optical satellite image pairs using convolutional neural networks (ConvNets), transformers, and a multi-task learning setup. However, transformers have not been leveraged for urban change detection with multi-temporal data, i.e.,  $> 2$  images, and multi-task learning methods lack integration approaches that combine change and segmentation outputs. To fill this research gap, we propose a continuous urban change detection method that identifies changes in each consecutive image pair of a satellite image time series. Specifically, we propose a temporal feature refinement (TFR) module that utilizes self-attention to improve ConvNet-based multi-temporal building representations. Furthermore, we propose a multi-task integration (MTI) module that utilizes Markov networks to find an optimal building map time series based on segmentation and dense change outputs. The proposed method effectively identifies urban changes based on high-resolution satellite image time series acquired by the PlanetScope constellation (F1 score 0.551) and Gaofen-2 (F1 score 0.440). Moreover, our experiments on two challenging datasets demonstrate the effectiveness of the proposed method compared to bi-temporal and multi-temporal urban change detection and segmentation methods. Code is available on GitHub: <https://github.com/SebastianHafner/ContUrbanCD>.

**Index Terms**—Earth observation, Remote sensing, Multi-temporal, Multi-task learning, Transformers

## I. INTRODUCTION

URBANIZATION is progressing at unprecedented rates [1]. Thus, the global amount of urban land is projected to increase by a factor of 2–6 over the 21st century [2]. The rapid expansion of urban land, i.e., urban sprawl, is associated with multiple negative effects on the environment and human well-being [3], [4]. To mitigate urban sprawl, informed and sustainable urban development strategies are crucial [5]. However, these strategies are currently hampered by a lack of timely information on the extent of urban land.

Remote sensing is an efficient tool to monitor the Earth’s surface [6]. Urban changes are commonly detected from two satellite images acquired at different times over the same geographical area. Traditional change detection methods use arithmetic operations to derive change features from bi-

temporal image pairs. For example, various arithmetic methods have been developed to derive change features from optical images, such as image differencing, image regression, and change vector analysis [7]. These features are then classified into changed/unchanged pixels or objects using different classification algorithms, including machine learning algorithms [6], [7].

In recent years, deep learning has been continuously replacing traditional change detection methods [8], [9]. Specifically, deep convolutional neural networks (ConvNets) have been used extensively for change detection in bi-temporal optical satellite image pairs (see Figure 1a). The simplest way of adapting common ConvNets such as U-Net [10] or HRNet [11] for change detection is with an input-level fusion (or early fusion [12]) strategy, referring to the concatenation of image pairs before passing them to a ConvNet. Contrarily, late fusion strategies typically process images separately in a Siamese network consisting of two ConvNets with shared weights. Extracted bi-temporal features are then fused using concatenation or absolute differencing [12], [13]. Since Siamese networks are generally considered preferable to input-level fusion strategies, multiple studies developed modules that are incorporated into Siamese network architectures to improve feature representations [14]–[16]. For very high-resolution (VHR) imagery, Chen *et al.* [17], [18] proposed to refine features extracted by ConvNets using a transformer-based module that alleviates the limited long-range context modeling capability of convolutions with self-attention. Since then, self-attention has become a popular mechanism for capturing long-range contextual information in VHR change detection [16], [19]–[21].

In recent years, high-resolution (i.e., 1 – 10 m) satellite image time series have become increasingly available [22]. Those data have enabled a shift from detecting land cover changes in image pairs acquired years apart to continuous annual and sub-annual change detection [23]. In contrast, urban change detection methods are predominantly designed for bi-temporal change detection from image pairs acquired multiple years apart [24]. However, considering the unprecedented rate of global urbanization [25], it is essential to develop a new suite of methods that detect urban changes continuously. While continuous change detection can be achieved by applying a bi-temporal model to consecutive image pairs in satellite image time series (see Figure 1c), this approach fails to exploit multi-temporal, i.e.,  $> 2$  images, information. Furthermore, recent studies [26], [27] have demonstrated the effectiveness of multi-

The authors are with the Division of Geoinformatics (Sebastian Hafner and Yifang Ban) and the Division of Robotics, Perception and Learning (Heng Fang and Hossein Azizpour) at KTH Royal Institute of Technology, 114 28 Stockholm, Sweden.

\*Corresponding author: Yifang Ban (e-mail: yifang@kth.se)

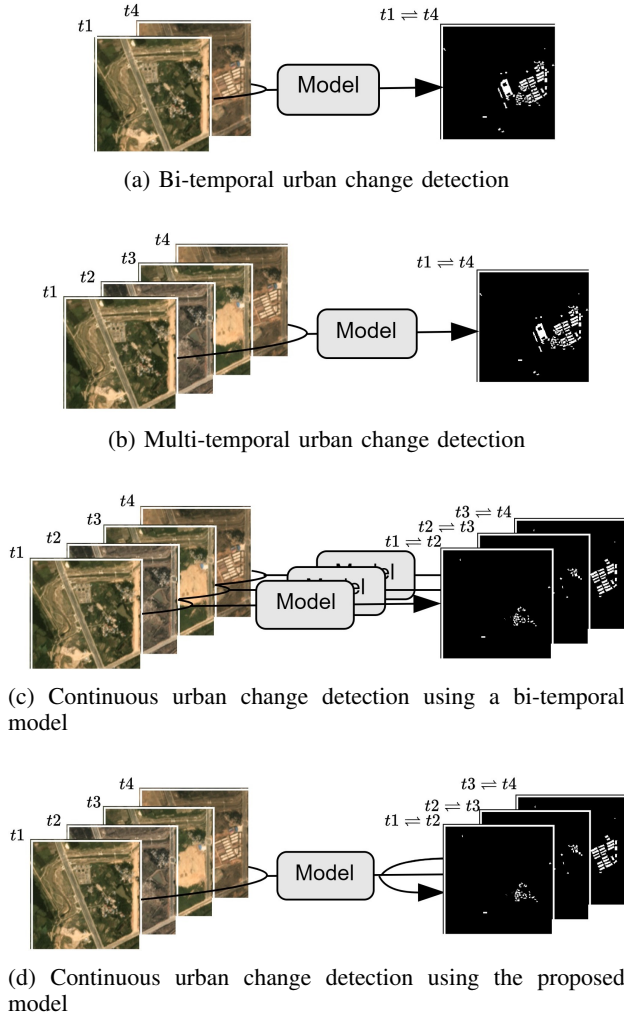


Fig. 1: Overview of standard urban change detection frameworks and the proposed method. (a) Bi-temporal urban change detection is typically performed on image pairs acquired multiple years apart. (b) Multi-temporal change detection methods leverage image time series but only predict changes between the first and last image. (c) A bi-temporal model is applied to consecutive image pairs of a time series to perform continuous urban change detection; however, this method fails to incorporate multi-temporal (i.e.,  $> 2$  images) information (c). On the other hand, we propose (d) a continuous urban change detection method that incorporates multi-temporal information.

temporal change detection models which predict changes between the first and last images of a satellite image time series (see Figure 1b). For example, multi-temporal information can help to reduce commission errors from registration errors, illumination differences, or other types of change unrelated to the problem of interest [27]. In addition, it can mitigate the effect of cloud artifacts in single images [26]. Existing multi-temporal change detection methods employ either recurrent layers, such as long short-term memory (LSTM) layers [28], or 3D convolutional layers to model temporal information [26], [27], [29], [30]. While these layers effectively model

short-range temporal dependencies in time series data, the self-attention mechanism can explicitly model temporal dependencies across all timestamps of a time series [31]. However, self-attention is predominately used in urban change detection to model long-range dependencies in space [16]–[19]. In contrast, this research aims to use self-attention to model multi-temporal information extracted from satellite image time series for urban change detection.

Another promising avenue of research for change detection is multi-task learning [32], where a related semantic segmentation task is trained parallel to the change detection task using a shared feature representation. The change detection task is commonly combined with building segmentation [27], [33]–[36] or land cover segmentation [37]–[39]. To that end, Siamese networks are extended with an additional decoder for the semantic segmentation task. The feature maps extracted by the encoder are then shared between the change decoder and the segmentation decoder. However, despite the attention multi-task learning has attracted in change detection, effective methods to integrate segmentation and change outputs have been largely unaddressed. For example, multi-task binary change detection studies consider building and change predictions independent outputs of the network [27], [33]–[36]. On the other hand, semantic change detection studies, concerned with identifying not only whether changes occurred (i.e., binary change detection) but also what types of changes occurred, apply a simple masking approach for multi-task integration [37]–[39]. Specifically, land cover predictions and binary change predictions are integrated by masking land cover changes derived from the bi-temporal semantic predictions with the binary change prediction. Therefore, existing multi-task change detection studies do not account for inconsistencies between the segmentation and change predictions. Moreover, these approaches fail to exploit the complementary information produced by multi-task predictions.

In this paper, we propose a continuous urban change detection method (see Figure 1d) and explore two research gaps in the current literature, namely (1) the use of the self-attention mechanism to model multi-temporal information in urban change detection and (2) the integration of segmentation and change predictions in multi-task learning setups. Specifically, we propose a new network architecture that relies on convolutions to extract multi-temporal building representations and employs self-attention to model temporal dependencies in feature space. We also propose a novel integration approach that determines the most likely state for each timestamp in a time series by considering multi-task predictions using Markov networks. The effectiveness of the proposed architecture and integration approach is demonstrated on two urban change detection datasets featuring high-resolution optical satellite image time series, namely the SpaceNet 7 dataset [40] and the Wuhan Urban Semantic Understanding (WUSU) dataset [41].

The following summarizes the main contributions of this paper.

- We present a transformer-based feature refinement module that effectively models temporal information in satellite image time series, leading to improved building

representations.

- We introduce a new multi-task integration approach that represents segmentation and change outputs in Markov networks to find the most likely building map for each image in a time series using *maximum a posteriori* (MAP) estimation.
- Experiments on two datasets, namely SpaceNet 7 and WUSU, show that the proposed continuous urban change detection method is more effective than related methods.

## II. RELATED WORK

### A. Bi-temporal change detection

In recent years, a plethora of deep learning-based bi-temporal change detection methods have been proposed. Most of these works focus on developing new Siamese network architectures and/or training strategies. Initially, Daudt *et al.* [12], [13] proposed two Siamese ConvNet architectures for change detection. The Siam-Diff and Siam-Conc architectures employ encoders with shared weights for feature extraction from bi-temporal high-resolution image pairs and combine the corresponding feature maps using a subtraction and concatenation strategy, respectively. While encoders and decoders in these models follow the U-Net architecture [10], Fang *et al.* [14] incorporated a nested U-Net (i.e., UNet++ [42]) into a Siamese network to maintain high-resolution fine-grained representations through dense skip connections. Many works also improved Siamese networks by incorporating different modules into the architecture. For example, an ensemble channel attention module was proposed for feature refinement in [14], and a new spatial pyramid pooling block was utilized in [15] to preserve shapes of change areas.

However, most recent methods are developed for bi-temporal change detection from VHR image pairs. Consequently, many methods employ the self-attention mechanism to improve the modeling of long-range dependencies in VHR imagery [16]–[19]. Both [17] and [18] extract image features with ConvNets and employ self-attention modules to learn more discriminative features. Other works combined ConvNets and transformers with attention modules and multi-scale processing [16], [43]. Bandara *et al.* [19], on the other hand, proposed a fully transformer-based change detection method. Specifically, ChangeFormer combines two hierarchically structured transformer encoders with shared weights and a multi-layer perception decoder in a Siamese network architecture. Since transformer-based methods strongly rely on pretraining, Noman *et al.* [21] recently proposed ScratchFormer which is a transformer-based change detection method that is trained from scratch but achieves SOTA performance. The ScratchFormer architecture utilizes shuffled sparse attention layers that enable faster convergence due to their sparse structure. Although these transformer-based methods are considered SOTA for urban change detection, their effectiveness has been predominately demonstrated on bi-temporal VHR datasets such as LEVIR-CD [17] and WHU-CD [44]. In comparison, high-resolution imagery is acquired much more frequently by satellite constellations such as PlanetScope, making it an invaluable data source for change detection applications.

Therefore, developing methods that effectively leverage transformers for change detection from high-resolution imagery is crucial.

### B. Change detection from satellite image time series

Few studies have developed deep learning methods for urban change detection from high-resolution satellite image time series. For example, Papadomanolaki *et al.* [26] proposed to incorporate LSTM networks into a U-Net model to leverage optical satellite image time series for change detection. Their L-UNet outperformed bi-temporal ConvNet-based methods on a bi-temporal dataset enriched with intermediate satellite images [26]. Others proposed an encoder-decoder LSTM model that is trained to rearrange temporally shuffled time series [30]. The core assumption of this unsupervised method is that the model fails to correctly rearrange shuffled data for changed pixels. Finally, Meshkini *et al.* [29] recently proposed a weakly supervised change detection method that employs 3D convolutional layers to capture spatial-temporal information in satellite image time series. Despite these promising results underlying the value of time series information, multi-temporal urban change detection methods may benefit from layers with better temporal modeling capabilities. Furthermore, most of these methods fail to detect urban changes continuously and are limited to the detection of changes between the first and the last image (i.e., multi-temporal change detection in Figure 1b).

### C. Multi-task learning

Multi-task learning has been investigated by several studies for urban change detection over the past years. Liu *et al.* [33] proposed a dual-task Siamese ConvNet to learn more discriminative feature representations for building change detection from bi-temporal image pairs. The proposed dual-task constrained deep Siamese convolutional network (DTCDCSCN) consists of three main components: a shared ResNet-based encoder, a shared decoder for building segmentation, and a separate decoder for change detection. On the other hand, Papadomanolaki *et al.* [27] proposed a multi-task learning framework for urban change detection from image time series by adding building segmentation tasks for the first and last images of a time series to the urban change detection task. While L-UNet [26] is employed to extract changes, the segmentation is performed with a separate decoder that directly uses the feature maps extracted for the image pair by the shared encoder.

Some urban change detection studies also combined multi-task learning with semi-supervised learning [34], [35]. In [34], the Siam-Diff network [13] was extended with an additional shared decoder for building segmentation, and an unsupervised term was introduced to encourage consistency between the changes derived from the building predictions and those predicted by the change decoder. Shu *et al.* [35], on the other hand, proposed to learn consistency between two building predictions corresponding to the pre-change image. The first prediction is obtained by segmenting the pre-change image and the second one by combining segmentation features of the post-change image with changes features.

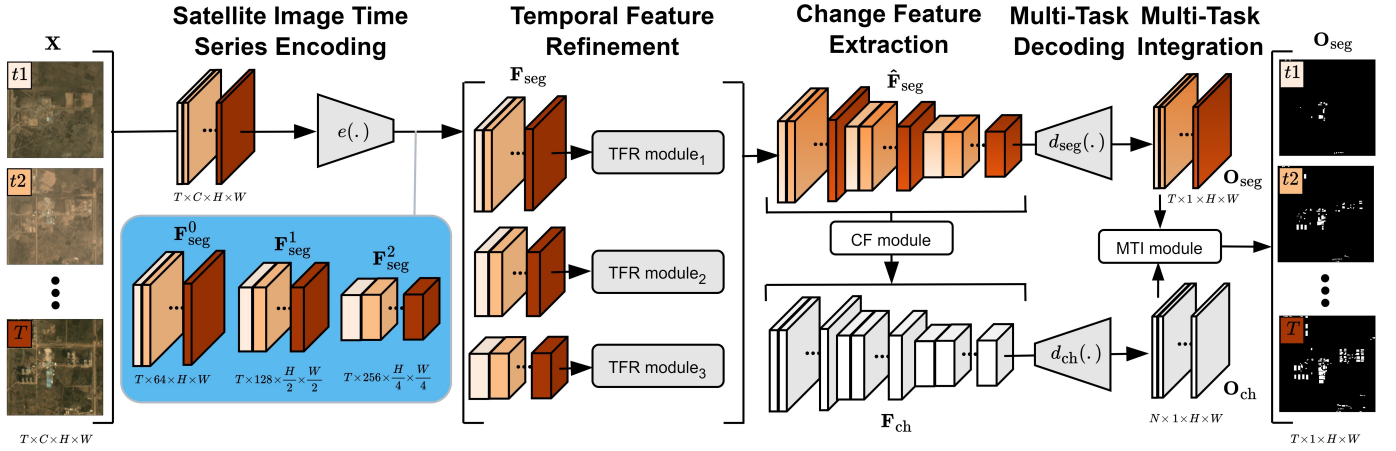


Fig. 2: Overview of the proposed method. First, an encoder extracts multi-scale feature maps from a satellite image time series. Next, transformer-based temporal feature refinement (TFR) modules enrich feature maps at each scale with multi-temporal information, and the change feature (CF) module generates bi-temporal difference feature maps from the temporally refined feature maps. Then, two separate decoders are used to obtain segmentation and change predictions from the respective feature maps. Finally, predictions for the two tasks are combined using a multi-task integration (MTI) module. For brevity, only three out of the five scales of the feature maps are shown.

Apart from binary change detection, multi-task learning has been employed for semantic change detection [37]–[39] and 3D change detection [20]. Daudt *et al.* [37] proposed a learning strategy that integrates change detection and land cover mapping from bi-temporal image pairs. Specifically, they propose a network consisting of separate encoder-decoder sub-networks for land cover mapping and binary change detection, where the change detection decoder also receives features from the mapping encoder in the form of difference skip connections. ChangeMask [38] uses a similar setup but introduces a transformer applied to the bi-temporal feature maps to learn more robust representations for the change task. Furthermore, [39] optimized semantic features in ChangeMask by adding a multi-task joint loss (i.e., ChangeMJ). Finally, Marsocci *et al.* [20] extended the bi-temporal image transformer (BIT) presented in [18] with a regression head to solve 2D and 3D change detection simultaneously using shared feature representations.

### III. THE PROPOSED METHOD

#### A. Overview

As illustrated in Figure 2, the main components of the proposed method are a ConvNet-based encoder, transformer-based temporal feature refinement (TFR) modules, a change feature (CF) module, two task-specific ConvNet-based decoders, and a Markovian multi-task (MTI) integration module. The following summarizes the urbanization monitoring process of the proposed method for a time series of satellite images:

1. First, for each image in the time series, multi-scale feature maps are extracted using an encoder with shared weights.
2. Next, the above time series of feature maps are grouped by scale and fed to separate TFR modules consisting of transformer encoder layers. The temporally refined feature maps are regrouped according to their timestamp.

3. Then, the CF module obtains change feature maps from the temporally refined segmentation feature maps. The module considers changes between all possible combinations of temporal pairs.
4. Two task-specific decoders are deployed to obtain building segmentation outputs for each image in the time series from the temporally refined segmentation features maps and change outputs from the change feature maps.
5. Finally, the building and urban change outputs are combined using the MTI module. The module uses pixel-wise Markov networks to obtain optimal building states for the satellite image time series.

Detailed descriptions of the components comprising the proposed method, as well as the loss function, are given in the following sections.

#### B. Satellite image time series encoding

We consider a time series of  $T$  satellite images, represented as  $\mathbf{X} \in \mathbb{R}^{T \times C \times H \times W}$ , where  $C$ ,  $H$ , and  $W$  denote the channel, height, and width dimensions, respectively. A ConvNet encoder with shared weights is utilized to separately extract feature maps  $\mathbf{F}_{\text{seg}}$  from each image in the time series, as follows:

$$\mathbf{F}_{\text{seg}} = e(\mathbf{X}), \quad (1)$$

where  $e(\cdot)$  represents the encoder, and subscript *seg* indicates that the feature maps contain representations for building segmentation.

The architecture of the encoder is based on the U-Net encoder [10]. Specifically, after an initial convolution block, the combination of a max-pooling layer and a consecutive convolution block is applied four times. Each of these four steps halves the spatial dimensions  $H$  and  $W$  due to the pooling operation, whereas the number of features  $D$  is doubled with

the convolution block. Importantly, U-Net achieves precise localization by leveraging skip connections that forward the feature maps before each pooling operation to the decoder. Therefore, the output of the encoder consists of five feature map time series with different scales. To denote the scale of these time series, we introduce superscript  $s$  in the notation:  $\mathbf{F}_{\text{seg}}^s$ , where  $s \in \{0, 1, 2, 3, 4\}$ . For a given feature map time series  $\mathbf{F}_{\text{seg}}^s$ , the sizes of the height and width dimensions, as well as the feature dimension, are dependent on  $s$ , as follows:

$$H^s = \frac{H}{2^s}, W^s = \frac{W}{2^s}, D^s = 64 \cdot 2^s. \quad (2)$$

It should be noted that for brevity, Figure 2 illustrates the proposed method for  $s \in \{0, 1, 2\}$ .

### C. Temporal feature refinement

The TFR module, illustrated in Figure 3, creates temporally refined feature maps using the self-attention mechanism along the temporal dimension [31]. Specifically, the module takes as input a time series of feature maps at the same scale  $s$  and reshapes this 4D tensor to a 3D tensor  $\mathbf{T}^s \in \mathbb{R}^{T \times D^s \times P^s}$  by flattening the spatial dimensions  $H^s$  and  $W^s$ . Consequently,  $T$ ,  $D$ , and  $P$  represent the temporal, feature embedding, and spatial dimensions, respectively.

After reshaping the feature map time series, self-attention is applied along the temporal dimension  $T$  for each cell in the spatial dimension  $P$ . However, since the self-attention mechanism contains no recurrence, it is necessary to first inject information about the temporal position of the feature vectors in the time series. Specifically, temporal encodings having the same dimension as the feature vectors are generated based on sine and cosine functions of different frequencies [31]. These relative temporal encodings are then added to the feature vectors.

The tensor, enriched with relative temporal position information, is passed through two transformer encoder layers (see Figure 4). The key component of the transformer encoder layer is the multi-head attention block, which performs self-attention defined as follows:

$$\text{Att}(\mathbf{Q}, \mathbf{K}, \mathbf{V}) = \text{softmax} \left( \frac{\mathbf{Q}\mathbf{K}^T}{\sqrt{D}} \right) \mathbf{V}, \quad (3)$$

where  $\mathbf{Q}$ ,  $\mathbf{K}$ , and  $\mathbf{V}$  are referred to as query, key, and value, respectively. The query-key-value triplet is computed with three linear projection layers with parameter matrices  $\mathbf{W}^Q, \mathbf{W}^K, \mathbf{W}^V \in \mathbb{R}^{D \times D}$  that are separately applied to a given cell of the 3D tensor  $\mathbf{T}_p^s$ , where  $p$  denotes the cell index in  $\mathbf{T}^s$ .

The core idea of multi-head attention is, however, that self-attention is performed multiple times in parallel using  $h$  attention heads, as follows:

$$\text{MultiHead}(\mathbf{Q}, \mathbf{K}, \mathbf{V}) = \text{Concat}(\text{head}_1, \dots, \text{head}_h) \mathbf{W}^O, \quad (4)$$

where  $\text{head}_i = \text{Att}(\mathbf{Q}\mathbf{W}_i^Q, \mathbf{K}\mathbf{W}_i^K, \mathbf{V}\mathbf{W}_i^V)$ .

Each head $_i$  performs self-attention on different projections of the keys, values, and queries obtained from linear layers

with parameter matrices  $\mathbf{W}_i^Q, \mathbf{W}_i^K, \mathbf{W}_i^V \in \mathbb{R}^{D \times D_{\text{head}}}$ . Finally, the concatenated outputs of the heads are reprojected using parameter matrix  $\mathbf{W}^O \in \mathbb{R}^{hD_{\text{head}} \times D}$ . We employ  $h = 2$  attention heads, where the head dimension is given by  $D_{\text{head}} = D/h$ .

After applying self-attention to each multi-temporal feature vector, we obtain a 3D tensor containing temporally refined building representations. In practice, however, all cells of tensor  $\mathbf{T}^s$  are processed in parallel by incorporating them into the batch dimension which is omitted for clarity. Finally, the 3D tensor is reshaped to the dimensions of the feature map time series by unflattening dimension  $P$ . We denote this temporally refined feature map time series with  $\hat{\mathbf{F}}_{\text{seg}}^s$ .

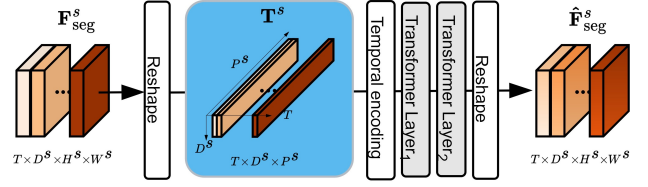


Fig. 3: Illustration of the temporal feature refinement (TFR) module.

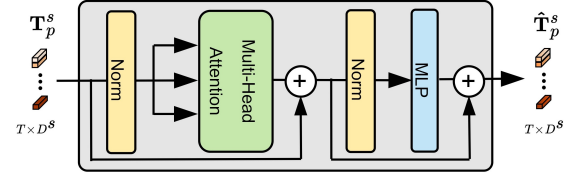


Fig. 4: Illustration of the transformer encoder layer applying multi-headed self-attention.

### D. Change feature extraction

The CF module is used to convert the temporally refined segmentation feature maps to change feature maps. Specifically, we consider the temporally refined feature maps  $\hat{\mathbf{F}}_{\text{seg}}^t$  and  $\hat{\mathbf{F}}_{\text{seg}}^k$ , corresponding to two images acquired at time  $t$  and time  $k$ , where  $1 \leq t < k \leq T$ . Then, change feature map  $\mathbf{F}_{\text{ch}}^n$  corresponding to the urban changes between the bi-temporal image pair is constructed as follows:

$$\mathbf{F}_{\text{ch}}^n = \hat{\mathbf{F}}_{\text{seg}}^k - \hat{\mathbf{F}}_{\text{seg}}^t, \quad (5)$$

where  $n$  denotes a change edge between timestamps  $t$  and  $k$ . It should be noted that this is done for each scale  $s$  of the feature maps.

This operation is identical to the change feature computation in the Siam-Diff method [13]. However, instead of only considering changes between the first and the last images of a time series, the CF module computes change feature maps for all possible combinations of image pairs. The total number of combinations  $N_{\text{dense}}$  is given by the length of the time series  $T$ , defined as follows:

$$N_{\text{dense}} = \frac{T(T-1)}{2}. \quad (6)$$

We refer to the scenario when all possible combinations of image pairs are considered as *dense*. However, we also investigate sparser settings such as *adjacent*, considering only changes between temporally adjacent images ( $N_{\text{adjacent}} = T - 1$ ), and *cyclic*, adding the changes between the first and last image to the adjacent setting ( $N_{\text{cyclic}} = T$ ) (see Figures 5a – 5c for visualizations of these settings in Markov networks with  $T = 5$ ). We provide ablation results on the different edge settings in Table III. Finally, it should be noted that the CF module does not have any trainable parameters.

### E. Multi-task decoding

Two separate decoders are deployed to convert the temporally enriched segmentation feature maps and the change feature maps to building outputs and urban change outputs, respectively. Formally, we obtain  $T$  built-up area segmentation outputs  $\mathbf{O}_{\text{seg}} \in (0, 1)^{T \times H \times W}$  with the segmentation decoder  $d_{\text{seg}}(\cdot)$  as follows:

$$\mathbf{O}_{\text{seg}} = d_{\text{seg}}(\hat{\mathbf{F}}_{\text{seg}}). \quad (7)$$

Furthermore, we obtain  $N$  change detection outputs  $\mathbf{O}_{\text{ch}} \in (0, 1)^{N \times H \times W}$  with the change decoder  $d_{\text{ch}}(\cdot)$  as follows:

$$\mathbf{O}_{\text{ch}} = d_{\text{ch}}(\mathbf{F}_{\text{ch}}). \quad (8)$$

Both decoders follow the architecture of the U-Net expansion path consisting of four upsampling blocks followed by a  $1 \times 1$  convolution layer and a sigmoid activation function. Upsampling blocks double the height and width of feature maps via a transpose conv  $2 \times 2$  layer. Upsampled feature maps are then concatenated along the channel dimension with the temporally refined feature maps matching their scale (skip connection). Subsequently, the layer triplet  $3 \times 3$  convolution, batch normalization, and ReLU activation is applied twice.

### F. Loss function

The network is trained using a loss function composed of two terms, namely for the urban change detection task ( $\mathcal{L}_{\text{ch}}$ ) and the building segmentation task ( $\mathcal{L}_{\text{seg}}$ ). For both loss terms, a Jaccard metric measuring the similarity between continuous network outputs  $\mathbf{O} \in (0, 1)$  and binary labels  $\mathbf{Y} \in \{0, 1\}$  is used [45]. We denote the Jaccard metric by  $J(\cdot)$  and define the loss function as follows:

$$\mathcal{L} = \sum_{t=1}^T J(\mathbf{O}_{\text{seg}}^t, \mathbf{Y}_{\text{seg}}^t) + \sum_{n=1}^N J(\mathbf{O}_{\text{ch}}^n, \mathbf{Y}_{\text{ch}}^n), \quad (9)$$

where  $T$  denotes the length of the time series and  $N$  denotes the number of edges (i.e., combinations of bi-temporal image pairs) considered. Segmentation and change labels are denoted by  $\mathbf{Y}_{\text{seg}} \in \{0, 1\}^{T \times H \times W}$  and  $\mathbf{Y}_{\text{ch}} \in \{0, 1\}^{N \times H \times W}$ , respectively. Specifically, we assume that pixel-wise building annotations,  $\mathbf{Y}_{\text{seg}}$ , are available and derive pixel-wise built-up changes,  $\mathbf{Y}_{\text{ch}}$ , according to the considered edges.

### G. Multi-task integration

To combine segmentation and change predictions, we propose the MTI module which determines the optimal building segmentation output for each image in a time series. Since this is a pixel-based approach, we represent the location of a specific pixel in the segmentation and change output notations by introducing superscript coordinates  $i$  and  $j$ . Following that,  $\mathbf{O}_{\text{seg}}^{(i,j),t}$  denotes the segmentation output for a specific pixel  $i, j$  at timestamp  $t$ , where  $i \in \{1, \dots, H\}$ ,  $j \in \{1, \dots, W\}$ , and  $t \in \{1, \dots, T\}$ . Likewise, the change output for a specific pixel is denoted by  $\mathbf{O}_{\text{ch}}^{(i,j),n}$ , where  $n$  denotes the change edge connecting timestamps  $t$  and  $k$ .

The core idea of the MTI module is to represent segmentation and change outputs in a pairwise Markov network. This subclass of Markov networks is associated with an undirected graph  $G = (\mathcal{N}, \mathcal{E})$  in which the nodes  $\mathcal{N}$  correspond to random variables and the edges  $\mathcal{E}$  represent pairwise relationships between the nodes (see [46]). For a given pixel, we construct a Markov network with  $T$  nodes corresponding to the timestamps in an image time series. Specifically, all nodes in the network correspond to a binary variable representing the presence of buildings (i.e.,  $\mathcal{N}^t \in \{true, false\}$ ). We use state 1 to denote *true*, representing the presence of a building, and state 0 to denote *false*, representing the absence of a building. Adjacent nodes in the network are connected with  $N - 1$  edges, where we use  $\mathcal{E}^{t=k}$  to denote an edge connecting timestamps  $t$  and  $k$ . We refer to this Markov network structure as an adjacent network (see Figure 5a).

To represent the segmentation and change outputs, the graph structure needs to be associated with a set of parameters that capture the relationships between nodes. The parameterization in a pairwise Markov network is achieved by assigning *factors* over nodes or edges, where a factor  $\phi$ , also referred to as *potential*, is a function from value assignments of random variables to real positive numbers  $\mathbb{R}^+$ . Thus, a pairwise Markov network is associated with a set of node potentials  $\{\phi(\mathcal{N}_t) : t = 1, \dots, T\}$  and a set of edge potentials  $\{\phi(\mathcal{N}_t, \mathcal{N}_k) : (\mathcal{N}_t, \mathcal{N}_k) \in G\}$ . The overall distribution represented by the network is then the normalized product of all the node and edge potentials.

The segmentation outputs for a specific pixel are incorporated into the Markov network by assigning a factor  $\phi_t$  over each node  $\mathcal{N}_t$ . Then, the segmentation outputs are encoded as node potentials, as follows:

$$\begin{aligned} \phi_t(\mathcal{N}^t = 1) &= \mathbf{O}_{\text{seg}}^{(i,j),t} \\ \phi_t(\mathcal{N}^t = 0) &= 1 - \mathbf{O}_{\text{seg}}^{(i,j),t}. \end{aligned} \quad (10)$$

These node potentials characterize the bias of nodes towards state 1 or 0, representing the presence or absence of a building, respectively. We refer to this Markov network as *degenerate* network, characterized by the absence of functions that capture the interactions between nodes.

To incorporate the change outputs for a specific pixel, we first include additional edges for the edge settings cyclic and dense. Specifically, for the cyclic case (Figures 5b), edge  $\mathcal{E}^{t1=T}$ , connecting the first node  $\mathcal{N}^{t1}$  and the last node  $\mathcal{N}^T$ ,

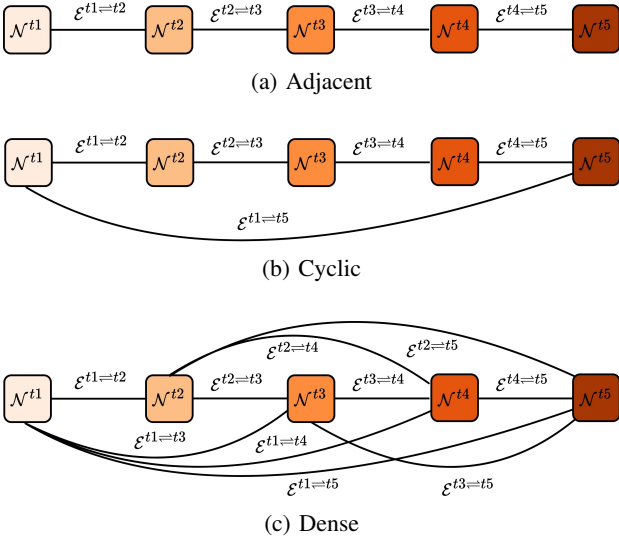


Fig. 5: Markov networks with different edge settings (exemplified for a time series with length  $T = 5$ ). Nodes and Edges are denoted by  $\mathcal{N}$  and  $\mathcal{E}$ , respectively.

is added. On the other hand, for the dense case (Figure 5c), all possible non-adjacent edges are added to the graph. Then, we define factors over the edges in the Markov network to add pairwise interactions of connected nodes. Specifically, we define pairwise potentials  $\phi_n$  for each edge  $\mathcal{E}^n$ , connecting two nodes  $\mathcal{N}^t$  and  $\mathcal{N}^k$ . Since all variables in the network are binary, each factor over an edge has four parameters. The change outputs are encoded as edge potentials for the four combinations of states, as follows:

$$\begin{aligned}
 \phi_n(\mathcal{N}^t = 0, \mathcal{N}^k = 1) &= \mathbf{O}_{\text{ch}}^{(i,j),n} \\
 \phi_n(\mathcal{N}^t = 1, \mathcal{N}^k = 0) &= \mathbf{O}_{\text{ch}}^{(i,j),n} \\
 \phi_n(\mathcal{N}^t = 0, \mathcal{N}^k = 0) &= 1 - \mathbf{O}_{\text{ch}}^{(i,j),n} \\
 \phi_n(\mathcal{N}^t = 1, \mathcal{N}^k = 1) &= 1 - \mathbf{O}_{\text{ch}}^{(i,j),n},
 \end{aligned} \tag{11}$$

where edge  $n$  is connecting timestamps  $t$  and  $k$ .

The value associated with each particular assignment of states denotes the affinity between the two states. Consequently, the higher the value assigned to the edge potential for a particular combination of states, the more compatible these two states are.

To define a global model from the local interactions defined in the parameterization of the Markov network, we take the product of the local factors and then normalize it. Once the distribution is defined, we perform a MAP query to find the most likely state assignment for each node in the graph. To that end, inference is performed using the belief propagation algorithm (see Algorithm 10.4 in [46]). Due to the absence of loops in the graph, belief propagation provides an exact solution. Finally, it should be noted that the MTI module does not contain any trainable parameters and is only deployed during inference.

## IV. EXPERIMENTAL SETTING

### A. Datasets

**SpaceNet 7:** The SpaceNet 7 dataset features time series of satellite images acquired by the PlanetScope constellation between 2017 and 2020 for 60 sites spread across the globe [41]. Each time series consists of about 24 monthly mosaics with a spatial resolution of 4 m (approximately  $1024 \times 1024$  pixels). Furthermore, the SpaceNet 7 dataset provides manually annotated building footprints, whereas annotations are missing for image parts affected by clouds. While the task of the original SpaceNet 7 challenge was to track these building footprints (i.e., vector data), the SpaceNet 7 dataset has been leveraged for a diverse set of tasks such as urban mapping [47], building counting [48], and urban change forecasting [49]. To split the SpaceNet 7 dataset into training, validation, and test areas, we apply the within-scene splits recommended in [48]. Specifically, approximately 80 % of a scene (top part) is used as a source of training patches, and the remaining 20 % (bottom part) is divided evenly into validation (bottom-left part) and test (bottom-right part) areas. Within-scene splits minimize the occurrence of out-of-distribution data during testing while simultaneously avoiding data leakage between the training and test set by utilizing spatially disjoint areas for the different dataset splits. During training, samples from the training areas are generated by randomly selecting  $T$  timestamps from the time series of a site. The rasterized building labels (see [34]) for these timestamps, were used to compute the change label. We draw 100 samples from each site during an epoch to reach an adequate number of steps before model evaluation. For model evaluation (validation and testing), the first and the last cloud-free images of a time series, in addition to evenly spaced intermediate images, were selected.

**WUSU:** The Wuhan Urban Semantic Understanding (WUSU) dataset features tri-temporal high-resolution Gaofen-2 images covering Wuhan's Hongshan District and Jiang'an District [39]. The preprocessing workflow of the satellite images includes orthographic correction and multi-temporal image registration. Furthermore, the four multi-spectral bands acquired at 4 m spatial resolution are pansharpened to a spatial resolution of 1 m, resulting in images of size  $6358 \times 6382$  and  $7025 \times 5500$  pixels for Hongshan District and Jiang'an District, respectively. In addition to the Gaofen-2 images, the WUSU dataset provides corresponding land-use/land-cover (LULC) labels, including manually refined building annotations (Class 2 Low building and Class 3 High building). Since the proposed method requires binary building labels, Class 2 and Class 3 were remapped to the foreground class, whereas all other classes were remapped to the background class. We follow the within-scene split recommended by the authors, using the top halves of the six images for the test set and the bottom halves for the training set that was further divided into training (90 %) and validation (10 %) tiles.

### B. Baseline and benchmark methods

We selected a comprehensive set of baseline and benchmark methods for quantitative and qualitative comparisons with the

proposed methods. These selected methods are listed under the categories bi-temporal change detection, multi-temporal change detection, and segmentation methods below.

#### Bi-temporal urban change detection methods

1. Siam-Diff [13] employs a Siamese encoder to extract feature maps from bi-temporal images. A decoder produces the change prediction from the subtracted feature maps. The encoders and decoder follow the U-Net architecture.
2. SNUNet [14] replaces the architecture in the Siam-Diff network with a Nested U-Net (UNet++ [42]). In addition, a channel attention module is incorporated into the architecture.
3. DTCDCSCN [33] combines a typical Siamese ConvNet for bi-temporal change detection with a dual attention module and two additional decoders with shared weights for building segmentation.
4. BIT [18] employs a bi-temporal image transformer module that operates in a compact token space to refine features extracted by a Siamese ConvNet.
5. AMTNet [16] also extracts features using a Siamese ConvNet, and combines attention mechanisms and multi-scale processing techniques to model contextual information in bi-temporal images.
6. ScratchFormer [21] introduces shuffled sparse attention layers in a Siamese ConvNet encoder to effectively capture semantic changes when training from scratch.

#### Multi-temporal urban change detection methods

7. L-UNet [26] combines a U-Net for feature extraction in image time series with LSTM modules [28] that obtain rich temporal information from the extracted feature maps.
8. Multi-Task L-UNet [27] adds a semantic decoder to L-UNet to segment buildings in the first and last images of a time series.

#### Building segmentation methods

9. U-Net [10] is an encoder-decoder ConvNet widely used for semantic segmentation tasks, including satellite image segmentation.
10. HRNet [50], or High-Resolution Net, is a ConvNet that maintains high-resolution representations through the whole network. For semantic segmentation, the high-resolution feature map is combined with the upsampled lower-resolution maps [11].

The Siamese ConvNets Siam-Diff, SNUNet, and DTCDCSCN are commonly used as change detection baselines, whereas BIT, AMTNet, and ScratchFormer represent recent methods combining Siamese ConvNets with transformers. On the other hand, L-UNet and Multi-Task L-UNet are benchmark methods for multi-temporal change detection. Finally, HRNet was employed by the winning approach of the SpaceNet 7 challenge for building segmentation, whereas U-Net was used as the baseline method [40]. Both methods also served as a LULC segmentation baseline for the WUSU dataset [39]. Finally, it should be noted that Multi-Task L-UNet and DTCDCSCN are multi-task methods that perform change detection and building segmentation.

#### C. Model evaluation

Two accuracy metrics were used for the quantitative assessment of predicted changes: F1 score and intersection over union (IoU). The combination of F1 score and IoU is commonly used for performance assessments in CD studies, e.g., [35], [36]. Formulas for the metrics are given in Eq. 12 and 13, where TP, FP, and FN represent the number of true positive, false positive, and false negative pixels, respectively.

$$\text{F1 score} = \frac{TP}{TP + \frac{1}{2}(FP + FN)} \quad (12)$$

$$\text{IoU} = \frac{TP}{TP + FP + FN}, \quad (13)$$

Using these two accuracy metrics, we assessed model performance across three tasks to accommodate the large variety of baseline and benchmark methods. These tasks are described in detail in the following:

- *Bi-temporal change detection* measures the accuracy of the predicted changes between the first and last image of a time series.
- *Continuous change detection* measures the average accuracy of the predicted changes between consecutive image pairs in a time series.
- *Segmentation* measures the accuracy of the building predictions corresponding to the first and last image of a time series.

The first task focuses on urban change detection from image pairs acquired multiple years apart. This task is considered by most urban change detection methods. For bi-temporal change detection methods, changes were directly predicted based on the first-last image pair, ignoring intermediate images in a time series. On the other hand, the second task focuses on assessing change predictions between consecutive image pairs in a time series. Consequently, the continuous urban change detection task focuses on image pairs with periods between acquisition dates that are considerably shorter (i.e., annual and sub-annual). The last task assesses the auxiliary segmentation task of multi-task methods and segmentation models. It should be noted that the change detection performance of segmentation models is not assessed because post-classification comparison suffers from the accumulation of classification errors [51].

#### D. Implementation details

We implement the proposed method using the deep learning framework PyTorch [52]. To efficiently reshape feature maps, we use the `rearrange` operation<sup>1</sup>. For the MTI module, we used the `pgmpy`<sup>2</sup> package to implement the Markov network and perform belief propagation. Models were trained for a maximum duration of 100 epochs on NVIDIA GeForce RTX 3080 graphics cards, using early stopping with patience 10 to prevent models from overfitting to the training set. AdamW was used as optimizer [53] with a linear learning rate scheduler. The remainder of this section describes the training setup in detail.

<sup>1</sup>See <https://einops.rocks/api/rearrange/>

<sup>2</sup>See <https://pgmpy.org/index.html>



**Augmentations:** To enhance the training dataset, we applied four data augmentation operations, namely rotations ( $k \cdot 90^\circ$ , where  $k$  is randomly selected from  $\{0, 1, 2, 3\}$ ), flips (horizontal and vertical with a probability of 50 %), Gaussian blur, and random color jittering. The parameters that determine how much to jitter the brightness, contrast, saturation, and hue of an image were set to 0.3 [19]. For validation and testing, on the other hand, no data augmentation was applied.

**Oversampling:** To account for the fact that the occurrence of change is usually considerably less frequent than no change [54], change areas were oversampled during network training. For a given site, twenty patches of size  $64 \times 64$  pixels were randomly cropped from the change label, before assigning each patch a probability according to its change pixel percentage, including a base probability for patches with no change pixels. A single patch was chosen based on those probabilities. For transformer-based methods (BIT, AMTNet, and Scratchformer), the patch size was increased to  $128 \times 128$  pixels to include more long-range spatial context.

**Hyper-parameter tuning:** For each model, hyper-parameters were tuned empirically on the validation set using grid search. Specifically, an exhaustive search with three learning rates ( $1 \cdot 10^{-5}$ ,  $5 \cdot 10^{-5}$ ,  $1 \cdot 10^{-4}$ ) and two batch sizes (8, 16) was performed to determine the optimum values of hyper-parameters. Then, five models were trained with the best hyper-parameters but different seeds for weight initialization and data shuffling. Consequently, reported values correspond to the average of five runs.

Multi-Task L-UNet requires additional hyper-parameters to balance the contribution of the segmentation and change loss terms, which we adopted from the paper [27]. All bi-temporal urban change detection methods were trained on the cyclic edges setting (see Figure 5b).

## V. EXPERIMENT RESULTS

In this section, we present the quantitative and qualitative results on the SpaceNet 7 and WUSU datasets, and the ablation study results. It should be noted that all accuracy values are reported on the respective test sets and correspond to the mean values obtained from five models. These were trained with different seeds using the best hyper-parameters determined with a grid search (see Section IV-D). On the other hand, the median model is used for the qualitative results.

### A. SpaceNet 7

The quantitative results for the SpaceNet 7 dataset are listed in Table I. The proposed method achieved the highest F1 scores and IoU values for both urban change detection tasks (i.e., bi-temporal and continuous). For bi-temporal change detection, methods using multi-temporal information (L-UNet and Multi-Task L-UNet) clearly outperform bi-temporal methods. Among the latter methods, the highest accuracy values were achieved by the ConvNet-based methods Siam-Diff and SNUNet, in addition to the transformer-based method ScratchFormer. For building segmentation, the best performance was also achieved by the proposed method, followed by the

TABLE I: Quantitative results on the SpaceNet 7 test areas. The best and second-best performance is highlighted in red and blue, respectively. ”-” denotes that the accuracy metric does not apply to a specific method since the corresponding variable is not predicted.

Method	Change detection				Segmentation	
	Bi-temporal		Continuous		F1	IoU
	F1	IoU	F1	IoU		
Siam-Diff	0.453	0.293	0.273	0.158	-	-
SNUNet	0.454	0.294	0.300	0.177	-	-
DTCDCSN	0.413	0.260	0.250	0.143	0.488	0.323
BIT	0.386	0.239	0.275	0.160	-	-
AMTNet	0.424	0.269	0.282	0.164	-	-
ScratchF.	0.469	0.306	<b>0.326</b>	<b>0.195</b>	-	-
L-UNet	<b>0.519</b>	<b>0.350</b>	-	-	-	-
MT L-UNet	0.515	0.347	-	-	0.512	0.344
U-Net	-	-	-	-	<b>0.527</b>	<b>0.359</b>
HRNet	-	-	-	-	<b>0.527</b>	0.358
Proposed	<b>0.551</b>	<b>0.381</b>	<b>0.414</b>	<b>0.261</b>	<b>0.596</b>	<b>0.424</b>

segmentation methods U-Net and HRNet and the multi-task methods Multi-Task L-UNet and DTCDCSN.

Qualitative results for the SpaceNet 7 dataset are shown for urban change detection and building segmentation in Figures 6 and 7, respectively. The change detection results are shown for test sites located in the United States, China, the Philippines, and Australia (top to bottom). Across these sites, the proposed method detects urban changes more accurately than other methods. For example, our method produces the fewest FP pixels (green) for the site located in the Philippines (third row). In addition, it reduces the number of FN pixels (magenta) compared to the other methods for the sites located in China (second row) and Australia (fourth row). The proposed method also accurately maps buildings, as demonstrated in Figure 7 for test sites located (from top to bottom) in the United States (first and second row), the Netherlands (third row), and Australia (fourth row).

### B. WUSU

The quantitative results for the WUSU datasets are listed in Table II. In general, change detection performance on the WUSU dataset is lower than on the SpaceNet 7 dataset. For bi-temporal change detection, only ScratchFormer, L-UNet, and the multi-task methods exceed an F1 score of 0.275 and an IoU value of 0.160. In comparison, accuracy values for the continuous change detection task are slightly higher, except for the proposed method. Overall, our method outperforms all other methods on both change detection tasks. For building segmentation, F1 scores of 0.500 and IoU values of 0.300 are exceeded by all methods with a segmentation output except Multi-Task L-UNet. U-Net and HRNet outperform the multi-task methods; however, the best results were achieved by the proposed method with an F1 score of 0.663 and an IoU value of 0.496.

Qualitative results for the WUSU dataset are shown for urban change detection and building segmentation in Figures 8

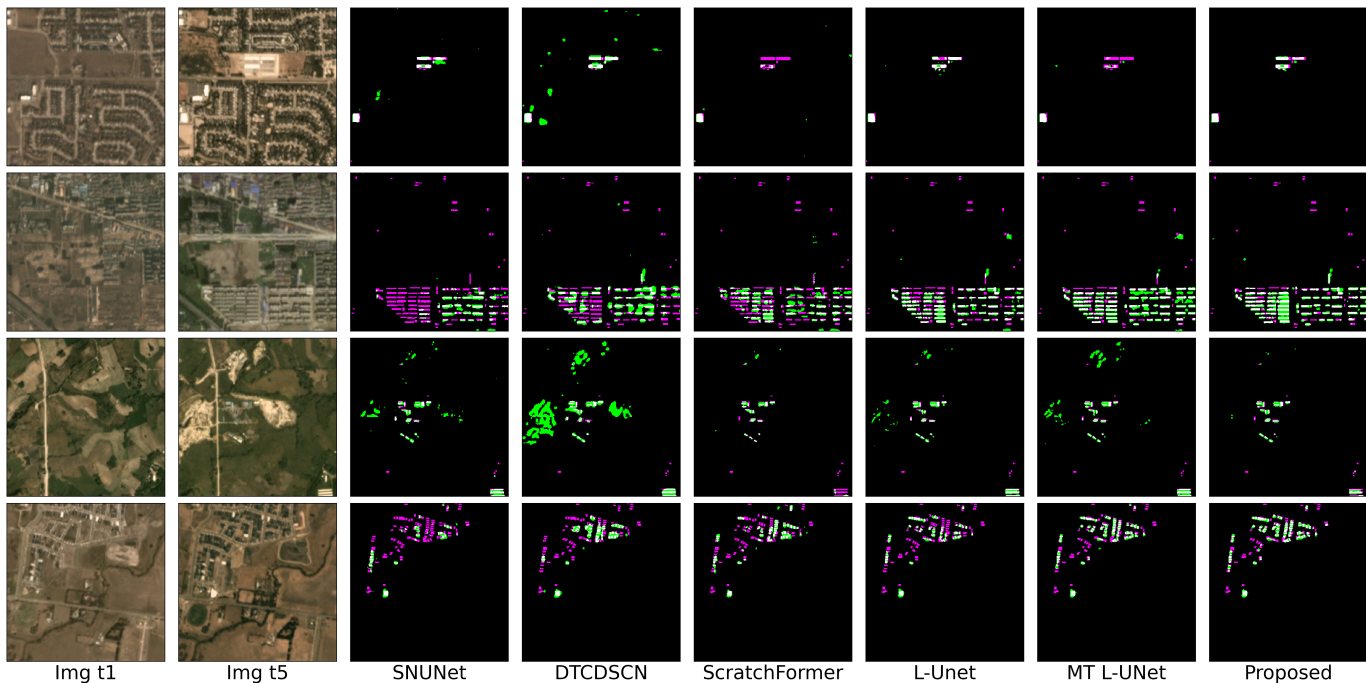


Fig. 6: Qualitative comparison of the predicted urban changes between the first (first column) and last (second column) image of a time series for a selection of the SpaceNet 7 test areas. Columns three to seven show the benchmarks and the last column shows the proposed method (White: TPs, Black: TNs, Green: FPs, and Magenta: FNs).

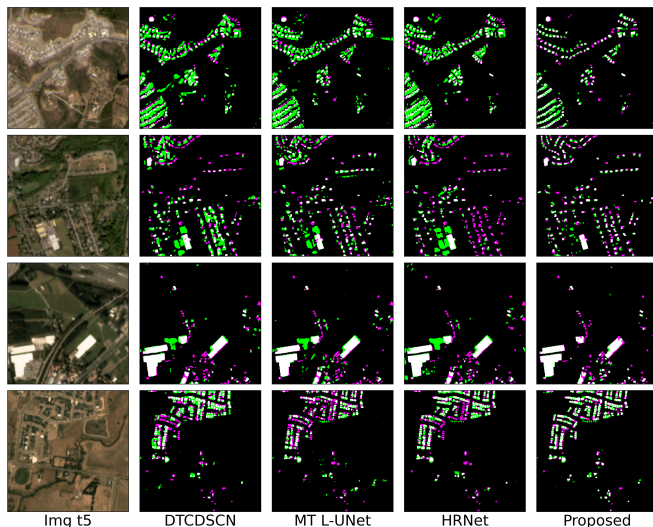


Fig. 7: Qualitative comparison of the built-up area predictions corresponding to the last image (first column) of a time series for a selection of the SpaceNet 7 test areas. Columns two to four show the benchmarks and the last column shows the proposed method (White: TPs, Black: TNs, Green: FPs, and Magenta: FNs).

and 9, respectively. All change detection methods considered in this visual comparison suffer from a large number of FN pixels (purple). In contrast, the proposed method is considerably more effective in detecting urban changes. In addition, the segmentation results for the last image in the time series (see Figure 9) demonstrate that the selected methods accurately

TABLE II: Quantitative results on the WUSU test areas. The best and second-best performance is highlighted in red and blue, respectively. "-" denotes that the accuracy metric does not apply to a specific method since the corresponding variable is not predicted.

Method	Change detection				Segmentation	
	Bi-temporal		Continuous		F1	IoU
	F1	IoU	F1	IoU		
Siam-Diff	0.175	0.096	0.236	0.134	-	-
SNUNet	0.188	0.104	0.211	0.118	-	-
DTCDSCN	0.278	0.162	0.318	0.189	0.539	0.369
BIT	0.213	0.120	0.314	0.187	-	-
AMTNet	0.187	0.104	0.264	0.152	-	-
ScratchF.	<b>0.324</b>	<b>0.193</b>	<b>0.353</b>	<b>0.214</b>	-	-
L-UNet	0.279	0.162	-	-	-	-
MT L-UNet	0.276	0.161	-	-	0.479	0.315
U-Net	-	-	-	-	0.576	0.406
HRNet	-	-	-	-	<b>0.611</b>	<b>0.440</b>
Proposed	<b>0.440</b>	<b>0.282</b>	<b>0.389</b>	<b>0.242</b>	<b>0.663</b>	<b>0.496</b>

map built-up area, even under challenging conditions with considerable off-nadir angles and shadows. Most incorrect predictions (FNs and FPs) are present at the edges of buildings, but a few buildings were also completely omitted. In general, the proposed method produces fewer FPs and FNs than the selected methods in this comparison.

### C. Ablation study

**Loss function and TFR module:** To measure the contribution of applying the loss function to additional change edges in

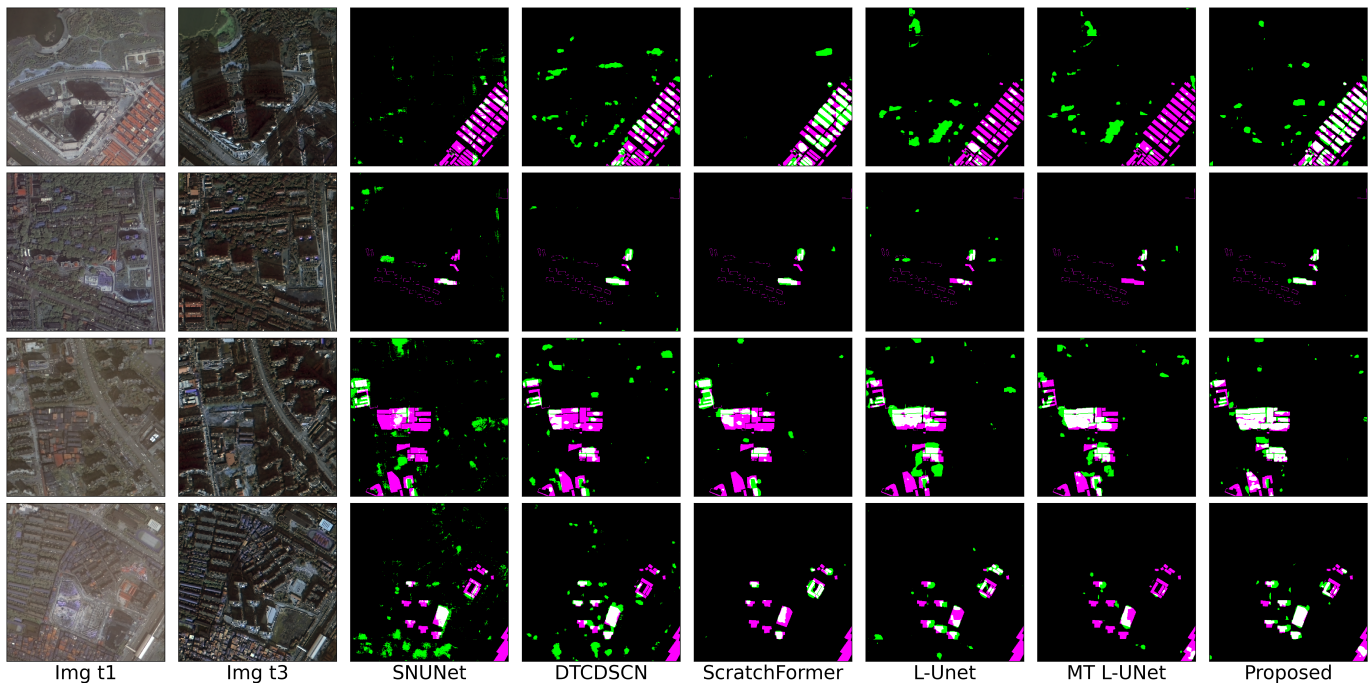


Fig. 8: Qualitative comparison of the predicted urban changes between the first (first column) and last (second column) image of a time series for a selection of the WUSU test areas. Columns three to seven show the benchmarks and the last column shows the proposed method (White: TPs, Black: TNs, Green: FPs, and Magenta: FNs).

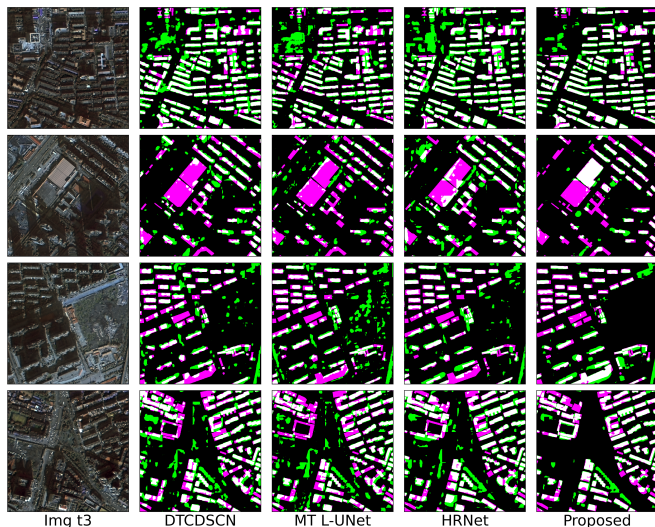


Fig. 9: Qualitative comparison of the built-up area predictions corresponding to the last image (first column) of a time series for a selection of the WUSU test areas. Columns two to four show the benchmarks and the last column shows the proposed method (White: TPs, Black: TNs, Green: FPs, and Magenta: FNs).

image time series, we perform an ablation experiment that tests different change loss settings on the SpaceNet 7 and WUSU datasets. Furthermore, we investigate the contribution of the TFR module by removing it from the model. The results listed in Table III show that adding change edges in the loss function generally improves performances of the segmentation and

change detection tasks. Regarding the TFR module, the results in Table III demonstrate a clear performance gain for both tasks from introducing transformer-based feature refinement. Specifically, adding the TFR module improves segmentation and change detection performance on both datasets considerably.

**MTI module:** We perform another ablation experiment investigating performance gains from leveraging additional edges in the MTI module. A degenerate Markov network that uses no change information (i.e., only the segmentation information represented as nodes) is added as a baseline. Table IV lists the ablation results for the SpaceNet 7 and WUSU datasets. Introducing change information in the MTI module results in considerable change detection performance gains compared to the degenerate setting while also providing minor segmentation performance gains. For example, using the adjacent setting improves change detection performance (first-last) by 44.8 % and 61.6 % in terms of F1 score and IoU, respectively, compared to the degenerate setting on the SpaceNet 7 dataset. On the WUSU dataset, the corresponding performance improvements are 57.5 % and 73.6 % for the F1 score and IoU, respectively (cyclic loss scenario). Table IV also shows that introducing change information beyond adjacent edges results in further change detection performance gains, albeit to a much lesser extent. For example, compared to only using adjacent change information, dense information improved the F1 score and IoU values by 2.0 % and 3.0 %, respectively. In the context of the WUSU dataset, additional change information (i.e., adjacent vs. cyclic) improved the F1 score and IoU values by 1.6 % and 2.2 %, respectively. Therefore, the ablation study demonstrates that the proposed MTI

TABLE III: Ablation results for the loss function and the TFR module on the SpaceNet 7 (SN7) and WUSU datasets. The change loss settings cyclic and dense are equivalent for the WUSU dataset since its time series consists of three images.

Dataset	Change loss	TFR module	Change detection				Segmentation	
			Bi-temporal		Continuous		F1	IoU
			F1	IoU	F1	IoU	F1	IoU
SN7	adjacent	✓	0.520	0.352	0.384	0.238	0.584	0.413
	cyclic	✓	0.532	0.363	0.377	0.233	0.581	0.409
	dense	✓	0.537	0.367	0.397	0.248	0.593	0.422
	dense	✗	0.490	0.324	0.314	0.186	0.549	0.379
WUSU	adjacent	✓	0.356	0.217	0.373	0.229	0.650	0.482
	cyclic	✓	0.420	0.266	0.391	0.243	0.660	0.493
	cyclic	✗	0.342	0.208	0.364	0.223	0.583	0.412

module effectively integrates the outputs of the segmentation and change detection tasks at inference time.

**Time series length:** To investigate the effect of satellite image time series length on performance, we tested the proposed network with different settings for  $T$ . For the change loss and MTI module, the maximum number of edges (i.e., dense edge setting) for a given  $T$  was used (see Equation 6). However, it should be noted that for lengths  $T = 3$  and  $T = 2$ , the edge settings dense are equivalent to cyclic and adjacent, respectively. The results of this experiment (Figure 10) show that adding intermediate images has a positive impact on bi-temporal change detection performance. Specifically, while the proposed method performed worse for  $T = 2$  compared to SOTA methods (Table I), our model outperforms these methods, including multi-temporal change detection methods, at longer time series lengths. Therefore, it effectively uses multi-temporal information to improve change detection performance.

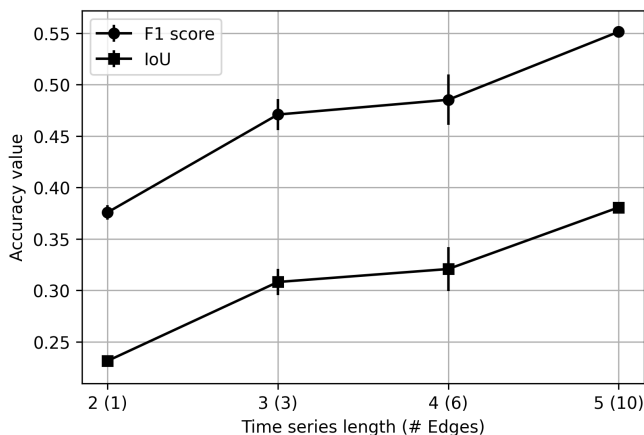


Fig. 10: The effect of time series length on bi-temporal change detection performance for the SpaceNet 7 dataset. The maximum number of edges was used for each time series length in the change loss and MTI module. Values represent the mean  $\pm 1$  standard deviation of 5 runs.

## VI. DISCUSSION

Our results highlight the challenging nature of continuously detecting urban changes from high-resolution satellite image

time series. Most methods are developed for bi-temporal urban change detection from VHR imagery, and SOTA methods have achieved remarkable results with F1 scores exceeding 0.9 on datasets such as LEVIR-CD [17] and WHU-CD [44]. In contrast, studies focusing on urban change detection from high-resolution imagery (e.g., PlanetScope or Sentinel-2) often fall short of F1 scores of 0.6, even when employing multi-task learning and multi-temporal data [27]. The suite of methods that achieved these impressive performances typically employs transformers to capture long-range contextual information in bi-temporal VHR imagery [16]–[19]. Our experiments indicate, however, that improving long-range context is less relevant in high-resolution imagery (Tables I and II). In addition, transformer-based methods rely heavily on pretraining on large datasets, which ScratchFormer successfully mitigates [21]. Furthermore, a recent study suggests that a simple segmentation ConvNet such as U-Net is still a top performer for change detection tasks [55]. We attribute those findings to the capability of modern ConvNets to capture sufficient spatial context in satellite imagery, especially when ground sampling distances are above 1 m. In comparison to the SOTA methods for bi-temporal change detection, our method leverages the self-attention mechanism to model multi-temporal information in satellite image time series. We showed that the proposed TFR module contributes to the network’s representation learning capability, resulting in improved change detection and semantic segmentation performance (Table III). Therefore, we deem self-attention an effective mechanism for feature refinement in continuous urban change detection networks.

Our work also highlights the need for effective integration approaches in multi-task learning schemes. Specifically, although multi-task learning is commonly applied for change detection [27], [33], existing multi-task studies do not address the integration of the semantic segmentation and change detection outputs. To fill this research gap, we proposed the MTI module that represents segmentation and change predictions using Markov networks to find the most likely built-up area state for each timestamp in a pixel time series. Our results demonstrate that the proposed integration approach improves both tasks, namely the change detection and building segmentation task (Table IV). Furthermore, we demonstrate that the proposed approach benefits from integrating dense change information, obtained from predicting changes between all possible combinations of satellite image pairs in a time

TABLE IV: Ablation results for the MTI module on the SpaceNet 7 and WUSU datasets. The change loss settings cyclic and dense are equivalent for the WUSU dataset since its time series consists of three images.

Dataset	Change loss	Edges	Change detection				Segmentation		
			Bi-temporal		Continuous		F1	IoU	
			F1	IoU	F1	IoU	F1	IoU	
SpaceNet 7	adjacent	degenerate	0.369	0.226	0.170	0.093	0.584	0.413	
		adjacent	0.533	0.363	0.398	0.248	0.586	0.415	
	cyclic	degenerate	0.362	0.221	0.164	0.089	0.581	0.409	
		adjacent	0.526	0.357	0.391	0.243	0.583	0.411	
		cyclic	0.535	0.366	0.394	0.246	0.583	0.412	
	dense	degenerate	0.373	0.229	0.173	0.095	0.593	0.422	
		adjacent	0.540	0.370	0.410	0.258	0.595	0.424	
		cyclic	0.547	0.377	0.412	0.260	0.596	0.424	
		dense	0.551	0.381	0.414	0.261	0.596	0.424	
	WUSU	adjacent	degenerate	0.244	0.139	0.186	0.103	0.650	0.482
			adjacent	0.409	0.257	0.368	0.226	0.656	0.488
		cyclic	degenerate	0.275	0.159	0.203	0.113	0.660	0.493
adjacent			0.433	0.276	0.389	0.242	0.663	0.497	
cyclic			0.440	0.282	0.389	0.242	0.663	0.496	
cyclic			0.440	0.282	0.389	0.242	0.663	0.496	

series, compared to using only adjacent change information (Table IV).

Despite the improvements our method achieves over existing methods, we also identified several limitations related to our work. First of all, our integration approach relies on meaningful potentials extracted from the multi-task network outputs. However, the outputs of deep networks may not be well-calibrated [56]. Furthermore, we assumed that our networks do not encounter out-of-distribution data during deployment due to the within-scene splits. In practice, however, urban mapping and change detection methods may encounter domain shifts when deployed to unseen geographic areas [36], [47]. Therefore, future work will test the susceptibility of our multi-task integration approach to out-of-distribution data. For example, the effectiveness of the MTI module could be improved by explicitly calibrating the segmentation and change outputs of the model, using calibration techniques such as temperature scaling [56].

Another limitation of the proposed method is that it requires continuous building labels for training. Most popular urban change detection datasets are bi-temporal and feature VHR imagery. On the other hand, few urban change detection datasets featuring satellite image time series and corresponding building labels for each image are available. Therefore, weakly supervised methods, using partial annotation or less accurate labeling, should be investigated for continuous urban change detection from satellite image time series (e.g., [29]).

## VII. CONCLUSION

In this study, we propose a continuous urban change detection method using optical satellite image time series. The proposed method leverages a transformer-based module to temporally refine feature representations extracted from image time series using a ConvNet. Furthermore, a new multi-task integration approach based on pairwise Markov networks is proposed to combine building segmentation and dense urban change information. We demonstrated the effectiveness of our

method on the SpaceNet 7 and WUSU datasets, where it outperformed existing bi-temporal and multi-temporal change detection methods and segmentation methods. The ablation study attributes these accuracy gains to the proposed TFR and MTI modules. Therefore, this research demonstrates the potential of high-resolution satellite image time series for the continuous detection of urban changes.

## ACKNOWLEDGEMENT

This work was supported by the EU Horizon 2020 project HARMONIA under agreement No. 101003517, Digital Futures under the grant for the EO-AI4GlobalChange project, and the EO-AI4Urban project within the ESA-MOST Dragon 5 Programme.

## REFERENCES

- [1] X. Liu, Y. Huang, X. Xu, X. Li, X. Li, P. Ciaes, P. Lin, K. Gong, A. D. Ziegler, A. Chen *et al.*, "High-spatiotemporal-resolution mapping of global urban change from 1985 to 2015," *Nature Sustainability*, pp. 1–7, 2020.
- [2] J. Gao and B. C. O'Neill, "Mapping global urban land for the 21st century with data-driven simulations and shared socioeconomic pathways," *Nature communications*, vol. 11, no. 1, p. 2302, 2020.
- [3] M. P. Johnson, "Environmental impacts of urban sprawl: a survey of the literature and proposed research agenda," *Environment and planning A*, vol. 33, no. 4, pp. 717–735, 2001.
- [4] S. A. Sarkodie, P. A. Owusu, and T. Leirvik, "Global effect of urban sprawl, industrialization, trade and economic development on carbon dioxide emissions," *Environmental Research Letters*, vol. 15, no. 3, p. 034049, 2020.
- [5] S. Arshad, S. R. Ahmad, S. Abbas, A. Asharf, N. A. Siddiqui, and Z. ul Islam, "Quantifying the contribution of diminishing green spaces and urban sprawl to urban heat island effect in a rapidly urbanizing metropolitan city of pakistan," *Land Use Policy*, vol. 113, p. 105874, 2022.
- [6] Y. Ban and O. Yousif, "Change detection techniques: A review," *Multi-temporal Remote Sensing*, pp. 19–43, 2016.
- [7] D. Lu, P. Mausel, E. Brondizio, and E. Moran, "Change detection techniques," *International journal of remote sensing*, vol. 25, no. 12, pp. 2365–2401, 2004.
- [8] X. X. Zhu, D. Tuia, L. Mou, G.-S. Xia, L. Zhang, F. Xu, and F. Fraundorfer, "Deep learning in remote sensing: A comprehensive review and list of resources," *IEEE Geoscience and Remote Sensing Magazine*, vol. 5, no. 4, pp. 8–36, 2017.

- [9] H. Jiang, M. Peng, Y. Zhong, H. Xie, Z. Hao, J. Lin, X. Ma, and X. Hu, "A survey on deep learning-based change detection from high-resolution remote sensing images," *Remote Sensing*, vol. 14, no. 7, p. 1552, 2022.
- [10] O. Ronneberger, P. Fischer, and T. Brox, "U-net: Convolutional networks for biomedical image segmentation," in *International Conference on Medical image computing and computer-assisted intervention*. Springer, 2015, pp. 234–241.
- [11] K. Sun, Y. Zhao, B. Jiang, T. Cheng, B. Xiao, D. Liu, Y. Mu, X. Wang, W. Liu, and J. Wang, "High-resolution representations for labeling pixels and regions," *arXiv preprint arXiv:1904.04514*, 2019.
- [12] R. C. Daudt, B. Le Saux, A. Boulch, and Y. Gousseau, "Urban change detection for multispectral earth observation using convolutional neural networks," in *IGARSS 2018-2018 IEEE International Geoscience and Remote Sensing Symposium*. IEEE, 2018, pp. 2115–2118.
- [13] R. C. Daudt, B. Le Saux, and A. Boulch, "Fully convolutional siamese networks for change detection," in *2018 25th IEEE International Conference on Image Processing (ICIP)*. IEEE, 2018, pp. 4063–4067.
- [14] S. Fang, K. Li, J. Shao, and Z. Li, "Snnnet-cd: A densely connected siamese network for change detection of vhr images," *IEEE Geoscience and Remote Sensing Letters*, vol. 19, pp. 1–5, 2021.
- [15] K. Basavaraju, N. Sravya, S. Lal, J. Nalini, C. S. Reddy, and F. Dell'Acqua, "Ucdnet: A deep learning model for urban change detection from bi-temporal multispectral Sentinel-2 satellite images," *IEEE Transactions on Geoscience and Remote Sensing*, 2022.
- [16] W. Liu, Y. Lin, W. Liu, Y. Yu, and J. Li, "An attention-based multiscale transformer network for remote sensing image change detection," *ISPRS Journal of Photogrammetry and Remote Sensing*, vol. 202, pp. 599–609, 2023.
- [17] H. Chen and Z. Shi, "A spatial-temporal attention-based method and a new dataset for remote sensing image change detection," *Remote Sensing*, vol. 12, no. 10, p. 1662, 2020.
- [18] H. Chen, Z. Qi, and Z. Shi, "Remote sensing image change detection with transformers," *IEEE Transactions on Geoscience and Remote Sensing*, vol. 60, pp. 1–14, 2021.
- [19] W. G. C. Bandara and V. M. Patel, "A transformer-based siamese network for change detection," in *IGARSS 2022-2022 IEEE International Geoscience and Remote Sensing Symposium*. IEEE, 2022, pp. 207–210.
- [20] V. Marsocci, V. Coletta, R. Ravanelli, S. Scardapane, and M. Crespi, "Inferring 3d change detection from bitemporal optical images," *ISPRS Journal of Photogrammetry and Remote Sensing*, vol. 196, pp. 325–339, 2023.
- [21] M. Noman, M. Fiaz, H. Cholakkal, S. Narayan, R. M. Anwer, S. Khan, and F. S. Khan, "Remote sensing change detection with transformers trained from scratch," *IEEE Transactions on Geoscience and Remote Sensing*, 2024.
- [22] D. P. Roy, H. Huang, R. Houborg, and V. S. Martins, "A global analysis of the temporal availability of planetscope high spatial resolution multi-spectral imagery," *Remote Sensing of Environment*, vol. 264, p. 112586, 2021.
- [23] Z. Zhu, S. Qiu, and S. Ye, "Remote sensing of land change: A multifaceted perspective," *Remote Sensing of Environment*, vol. 282, p. 113266, 2022.
- [24] A. Shafique, G. Cao, Z. Khan, M. Asad, and M. Aslam, "Deep learning-based change detection in remote sensing images: A review," *Remote Sensing*, vol. 14, no. 4, p. 871, 2022.
- [25] X. Liu, G. Hu, Y. Chen, X. Li, X. Xu, S. Li, F. Pei, and S. Wang, "High-resolution multi-temporal mapping of global urban land using Landsat images based on the Google Earth Engine platform," *Remote sensing of environment*, vol. 209, pp. 227–239, 2018.
- [26] M. Papadomanolaki, S. Verma, M. Vakalopoulou, S. Gupta, and K. Karantzas, "Detecting urban changes with recurrent neural networks from multitemporal Sentinel-2 data," in *IGARSS 2019-2019 IEEE International Geoscience and Remote Sensing Symposium*. IEEE, 2019, pp. 214–217.
- [27] M. Papadomanolaki, M. Vakalopoulou, and K. Karantzas, "A deep multitask learning framework coupling semantic segmentation and fully convolutional LSTM networks for urban change detection," *IEEE Transactions on Geoscience and Remote Sensing*, vol. 59, no. 9, pp. 7651–7668, 2021.
- [28] S. Hochreiter and J. Schmidhuber, "Long short-term memory," *Neural computation*, vol. 9, no. 8, pp. 1735–1780, 1997.
- [29] K. Meshkini, F. Bovolo, and L. Bruzzone, "Multi-annual change detection using a weakly supervised 3d cnn in hr sats," *IEEE Geoscience and Remote Sensing Letters*, pp. 1–1, 2024.
- [30] S. Saha, F. Bovolo, and L. Bruzzone, "Change detection in image time-series using unsupervised LSTM," *IEEE Geoscience and Remote Sensing Letters*, 2020.
- [31] A. Vaswani, N. Shazeer, N. Parmar, J. Uszkoreit, L. Jones, A. N. Gomez, Ł. Kaiser, and I. Polosukhin, "Attention is all you need," *Advances in neural information processing systems*, vol. 30, 2017.
- [32] R. Caruana, "Multitask learning," *Machine learning*, vol. 28, pp. 41–75, 1997.
- [33] Y. Liu, C. Pang, Z. Zhan, X. Zhang, and X. Yang, "Building change detection for remote sensing images using a dual-task constrained deep siamese convolutional network model," *IEEE Geoscience and Remote Sensing Letters*, vol. 18, no. 5, pp. 811–815, 2020.
- [34] S. Hafner, Y. Ban, and A. Nascetti, "Urban change detection using a dual-task siamese network and semi-supervised learning," in *IGARSS 2022-2022 IEEE International Geoscience and Remote Sensing Symposium*. IEEE, 2022, pp. 1071–1074.
- [35] Q. Shu, J. Pan, Z. Zhang, and M. Wang, "Mtcnet: Multitask consistency network with single temporal supervision for semi-supervised building change detection," *International Journal of Applied Earth Observation and Geoinformation*, vol. 115, p. 103110, 2022.
- [36] S. Hafner, Y. Ban, and A. Nascetti, "Semi-supervised urban change detection using multi-modal sentinel-1 sar and sentinel-2 msi data," *Remote Sensing*, vol. 15, no. 21, p. 5135, 2023.
- [37] R. C. Daudt, B. Le Saux, A. Boulch, and Y. Gousseau, "Multitask learning for large-scale semantic change detection," *Computer Vision and Image Understanding*, vol. 187, p. 102783, 2019.
- [38] Z. Zheng, Y. Zhong, S. Tian, A. Ma, and L. Zhang, "Changemask: Deep multi-task encoder-transformer-decoder architecture for semantic change detection," *ISPRS Journal of Photogrammetry and Remote Sensing*, vol. 183, pp. 228–239, 2022.
- [39] S. Shi, Y. Zhong, Y. Liu, J. Wang, Y. Wan, J. Zhao, P. Lv, L. Zhang, and D. Li, "Multi-temporal urban semantic understanding based on gf-2 remote sensing imagery: from tri-temporal datasets to multi-task mapping," *International Journal of Digital Earth*, vol. 16, pp. 3321–3347, 2023.
- [40] A. Van Etten and D. Hogan, "The spacenet multi-temporal urban development challenge," *arXiv preprint arXiv:2102.11958*, 2021.
- [41] A. Van Etten, D. Hogan, J. Martinez-Manso, J. Shermeyer, N. Weir, and R. Lewis, "The multi-temporal urban development SpaceNet dataset," *arXiv preprint arXiv:2102.04420*, 2021.
- [42] Z. Zhou, M. M. Rahman Siddiquee, N. Tajbakhsh, and J. Liang, "Unet++: A nested u-net architecture for medical image segmentation," in *Deep Learning in Medical Image Analysis and Multimodal Learning for Clinical Decision Support: 4th International Workshop, DLMIA 2018, and 8th International Workshop, ML-CDS 2018, Held in Conjunction with MICCAI 2018, Granada, Spain, September 20, 2018, Proceedings 4*. Springer, 2018, pp. 3–11.
- [43] L. Wang, J. Zhang, Q. Guo, and D. Chen, "Ifstdnet: An interact-feature transformer network with spatial detail enhancement module for change detection," *IEEE Geoscience and Remote Sensing Letters*, 2023.
- [44] S. Ji, S. Wei, and M. Lu, "Fully convolutional networks for multisource building extraction from an open aerial and satellite imagery data set," *IEEE Transactions on Geoscience and Remote Sensing*, vol. 57, no. 1, pp. 574–586, 2018.
- [45] D. Duque-Arias, S. Velasco-Forero, J.-E. Deschaut, F. Goulette, A. Serna, E. Decencièrre, and B. Marcotegui, "On power Jaccard losses for semantic segmentation," in *VISAPP 2021: 16th International Conference on Computer Vision Theory and Applications*, 2021.
- [46] D. Koller and N. Friedman, *Probabilistic graphical models: principles and techniques*. MIT press, 2009.
- [47] S. Hafner, Y. Ban, and A. Nascetti, "Unsupervised domain adaptation for global urban extraction using sentinel-1 sar and sentinel-2 msi data," *Remote Sensing of Environment*, vol. 280, p. 113192, 2022.
- [48] M. T. Razzak, G. Mateo-García, G. Lecuyer, L. Gómez-Chova, Y. Gal, and F. Kalaitzis, "Multi-spectral multi-image super-resolution of sentinel-2 with radiometric consistency losses and its effect on building delineation," *ISPRS Journal of Photogrammetry and Remote Sensing*, vol. 195, pp. 1–13, 2023.
- [49] N. Metzger, M. Ö. Türkoglu, R. C. Daudt, J. D. Wegner, and K. Schindler, "Urban change forecasting from satellite images," *PFG—Journal of Photogrammetry, Remote Sensing and Geoinformation Science*, pp. 1–10, 2023.
- [50] J. Wang, K. Sun, T. Cheng, B. Jiang, C. Deng, Y. Zhao, D. Liu, Y. Mu, M. Tan, X. Wang *et al.*, "Deep high-resolution representation learning for visual recognition," *IEEE transactions on pattern analysis and machine intelligence*, vol. 43, no. 10, pp. 3349–3364, 2020.
- [51] S. Liu, H. Su, G. Cao, S. Wang, and Q. Guan, "Learning from data: A post classification method for annual land cover analysis in urban areas," *ISPRS Journal of Photogrammetry and Remote Sensing*, vol. 154, pp. 202–215, 2019.

- [52] A. Paszke, S. Gross, F. Massa, A. Lerer, J. Bradbury, G. Chanan, T. Killeen, Z. Lin, N. Gimeshin, L. Antiga *et al.*, “Pytorch: An imperative style, high-performance deep learning library,” *arXiv preprint arXiv:1912.01703*, 2019.
- [53] I. Loshchilov and F. Hutter, “Fixing weight decay regularization in adam,” 2018.
- [54] F. Bovolo and L. Bruzzone, “The time variable in data fusion: A change detection perspective,” *IEEE Geoscience and Remote Sensing Magazine*, vol. 3, no. 3, pp. 8–26, 2015.
- [55] I. Corley, C. Robinson, and A. Ortiz, “A change detection reality check,” *arXiv preprint arXiv:2402.06994*, 2024.
- [56] C. Guo, G. Pleiss, Y. Sun, and K. Q. Weinberger, “On calibration of modern neural networks,” in *International conference on machine learning*. PMLR, 2017, pp. 1321–1330.